Aspartate all-in-one doping strategy enables efficient all-perovskite tandems

https://doi.org/10.1038/s41586-023-06707-z

Received: 17 May 2023

Accepted: 3 October 2023

Published online: 08 November 2023

Check for updates

Shun Zhou[1,2], Shiqiang Fu[1,2], Chen Wang[1,2], Weiwei Meng[1], Jin Zhou[1], Yuanrong Zou[1], Qingxian Lin[1], Lishuai Huang[1], Wenjun Zhang[1], Guojun Zeng[1], Dexin Pu[1], Hongling Guan[1], Cheng Wang[1], Kailian Dong[1], Hongsen Cui[1], Shuxin Wang[1], Ti Wang[1], Guojia Fang[1]✉ & Weijun Ke[1]✉

All-perovskite tandem solar cells hold great promise in surpassing the Shockley–Queisser limit for single-junction solar cells[1–3]. However, the practical use of these cells is currently hampered by the subpar performance and stability issues associated with mixed tin–lead (Sn–Pb) narrow-bandgap perovskite subcells in all-perovskite tandems[4–7]. In this study, we focus on the narrow-bandgap subcells and develop an all-in-one doping strategy for them. We introduce aspartate hydrochloride (AspCl) into both the bottom poly(3,4-ethylene dioxythiophene)–poly(styrene sulfonate) and bulk perovskite layers, followed by another AspCl posttreatment. We show that a single AspCl additive can effectively passivate defects, reduce Sn^{4+} impurities and shift the Fermi energy level. Additionally, the strong molecular bonding of AspCl–Sn/Pb iodide and AspCl–AspCl can strengthen the structure and thereby improve the stability of Sn–Pb perovskites. Ultimately, the implementation of AspCl doping in Sn–Pb perovskite solar cells yielded power conversion efficiencies of 22.46% for single-junction cells and 27.84% (27.62% stabilized and 27.34% certified) for tandems with 95% retention after being stored in an N_2-filled glovebox for 2,000 h. These results suggest that all-in-one AspCl doping is a favourable strategy for enhancing the efficiency and stability of single-junction Sn–Pb perovskite solar cells and their tandems.

Over the past decade, organometal halide perovskite materials (ABX_3) have emerged as promising options for light-absorbing materials in photovoltaic technologies[8]. To achieve narrow bandgaps (NBGs) for single-junction solar cells, and indeed for subcells for all-perovskite tandems, in the range of 1.1–1.4 eV, lead (Pb) and tin (Sn) can be alloyed in B-site metal ions[9]. However, fabricating high-efficiency and stable NBG tin–lead (Sn–Pb) perovskite solar cells (PSCs) remains a substantial challenge due to the easy oxidation of Sn^{2+} to Sn^{4+}, which leads to p-type self-doping, short carrier lifetimes and device performance degradation[6,10]. To address this issue, various strategies, including the use of multiple additives in the device fabrication process, have been proposed to improve the performance of mixed Sn–Pb PSCs[5,11,12]. Record performance of all-perovskite tandem cells has been achieved by optimizing both NBG mixed Sn–Pb subcells and wide-bandgap (WBG) subcells[2,13–16]. However, there is still significant scope for improving the performance of single-junction Sn–Pb PSCs, which ultimately determines the ceiling of all-perovskite tandems[5].

Mechanism of aspartate all-in-one doping

We developed an all-in-one doping method for Sn–Pb PSCs by incorporating a chiral aspartate hydrochloride (AspCl) molecule into the bottom poly(3,4-ethylene dioxythiophene)–poly(styrene sulfonate) PEDOT:PSS (PEDOT), middle perovskite light-absorbing layers (Bulk), and top capping layers (POST) (Fig. 1a). The AspCl molecule consists of three functional moieties (Fig. 1b). The Cl^- anion suppresses the formation of iodine vacancies[17,18], the amino group coordinates with I^- to reduce trap states and suppress iodide ion migration[18–20], and the carboxyl group coordinates with Pb and Sn ions to suppress perovskite decomposition[19,21,22]. Moreover, the amino and carboxyl groups in two AspCl molecules can be bound to each other by intermolecular hydrogen bonding in the bulk of perovskite films and interfaces of perovskite/bottom hole transport layers (HTLs) and perovskite/top capping layer. Therefore, this AspCl doping strategy creates an internal molecule lock for perovskites (Fig. 1c), which could efficiently passivate surface defects and improve device stability.

To support this hypothesis, we employed density functional theory (DFT) to calculate the potential alignment orientations of AspCl in various scenarios. We found that all the bonding energies are negative, signifying the energetically favourable formation of these bonds and suggesting that AspCl aligns parallel to perovskites, fullerene (C_{60}) and PEDOT:PSS (Supplementary Figs. 1 and 2 and Supplementary Table 1). Furthermore, we conducted DFT calculations to study the potential molecular interactions. We found that the bonding energies of AspCl–tin (II) iodide (-SnI_2) and AspCl–lead iodide (-PbI_2) are lower than that of formamidinium iodide (FAI)–SnI_2 and FAI–PbI_2, suggesting the more favourable formation of AspCl–SnI_2 and AspCl–PbI_2 than that of FAI–SnI_2 and FAI–PbI_2 (Supplementary Figs. 3 and 4 and

[1]Key Lab of Artificial Micro- and Nano-Structures of Ministry of Education, School of Physics and Technology, Wuhan University, Wuhan, China. [2]These authors contributed equally: Shun Zhou, Shiqiang Fu, Chen Wang. ✉e-mail: gjfang@whu.edu.cn; weijun.ke@whu.edu.cn

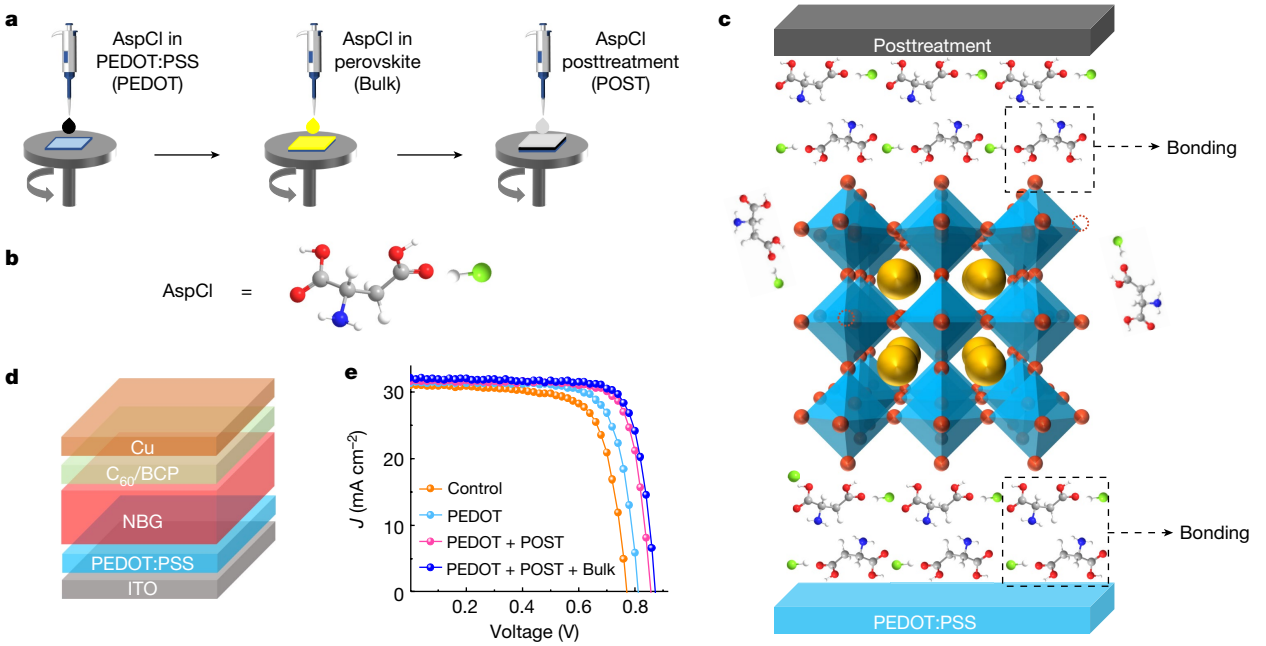

Fig. 1 | Preparation and mechanism of AspCl in NBG Sn–Pb perovskites. **a**, Schematic of device fabrication processes. PEDOT, Bulk and POST are defined as being doped with AspCl in PEDOT:PSS, and bulk perovskite precursors and for posttreatment on top of perovskite layers, respectively. **b**, Ball-and-stick model of AspCl. **c**, Mechanism diagram of AspCl modification at different positions within the devices. Bonding indicates the interaction between perovskite and AspCl or among AspCl molecules. Posttreatment involves applying a top capping layer of AspCl onto the perovskite film surface. **d**, Device structure diagram of NBG solar cells. **e**, *J*–*V* curves of NBG solar cells under various AspCl treatment conditions. BCP, bathocuproine; ITO, indium tin oxide.

Supplementary Tables 2 and 3). In addition to its ability to coordinate with metal halides, AspCl also has strong intermolecular hydrogen bonding. The coordination energy of AspCl–AspCl is lower than that of AspCl–FAI and FAI–FAI (Supplementary Table 3), indicating that AspCl is also favoured to interact with itself and can act as a 'lock' molecule between the perovskite layers and interfaces. Therefore, the results suggest that the introduction of AspCl could be conducive to passivating defects, suppressing ion migration and stabilizing perovskites.

To evaluate the effectiveness of AspCl in Sn–Pb perovskite devices, we fabricated single-junction Sn–Pb PSCs (Fig. 1d) and tested their performance under different treatment conditions (Fig. 1e and Supplementary Tables 4 and 5). After optimization, the concentrations of AspCl for PEDOT, Bulk, and POST treatments were 4 mg ml^{-1}, 0.2 mg ml^{-1}, and 1 mol%, respectively (Supplementary Figs. 5–7). The results showed that AspCl incorporation could significantly improve the device performance, and the device with integrated PEDOT + POST + Bulk AspCl modifications exhibited the best performance.

Characterization of NBG Sn–Pb perovskites

We then conducted a series of characterizations to investigate the factors contributing to the performance enhancements. The film morphology was initially evaluated by conducting scanning electron microscopy (SEM) measurements. As demonstrated in Fig. 2a,b and Supplementary Fig. 8, all films exhibited similar grain sizes, but there were marked differences in the grain boundaries, which were also confirmed by atomic force microscopy (AFM) measurements (Supplementary Fig. 9). The control film displayed bright particles at the grain boundaries, primarily from excess PbI_2 content[23,24]. It should be noted that lead thiocyanate was employed in the film precursors to enlarge perovskite grains[25], which contributed to the excessive PbI_2 at the grain boundaries. However, none of the other three samples showed an excess of PbI_2, which is beneficial for enhancing device performance since the absence of excessive PbI_2 in perovskite films can reduce hysteresis behaviour and improve device stability[23,24,26].

To further investigate the crystalline quality of the films, we performed X-ray diffraction (XRD) measurements. As depicted in Fig. 2c and Supplementary Fig. 10, all XRD patterns displayed similar characteristic peaks and peak positions, indicating that AspCl did not change the crystal structure. Consistent with the SEM results, only the control sample showed an additional peak at 12.7° (Supplementary Fig. 11), corresponding to the (001) peak of PbI_2 (ref. 27). Hence, the introduction of AspCl could mitigate the surplus presence of PbI_2 within the perovskite films (Supplementary Fig. 12). Moreover, no additional peaks were observed below 10°, implying that no significant low-dimensional perovskites were formed (Supplementary Fig. 11). Even with large amounts of AspCl, no diffraction peaks were detected for low-dimensional perovskites in the films (Supplementary Fig. 13). The XRD intensity of the perovskite films decreased gradually with increasing AspCl in both perovskite and posttreatment precursors, confirming that excessive AspCl could impede crystal growth. As depicted in Supplementary Figs. 3, 4 and 14 and Supplementary Tables 2 and 3, AspCl exhibits a robust affinity towards metal halide salts. Consequently, the introduction of AspCl introduces a dynamic where competition emerges between the formation of perovskites and AspCl–SnI_2/PbI_2 complexes. Notably, Sn–Pb perovskites are known for their rapid crystallization rate, a characteristic that can potentially compromise film quality[28,29]. In this context, the judicious use of AspCl in modest quantities can aptly moderate the rapid crystallization rate of Sn–Pb perovskites. Thus, an excessive application of AspCl negatively impacts the crystalline quality of the films.

Ultraviolet-visible (UV-vis) absorption spectra showed that perovskite films incorporating AspCl had slightly stronger absorption compared with the control sample (Supplementary Fig. 15). This enhancement can be mainly attributed to the improved film quality

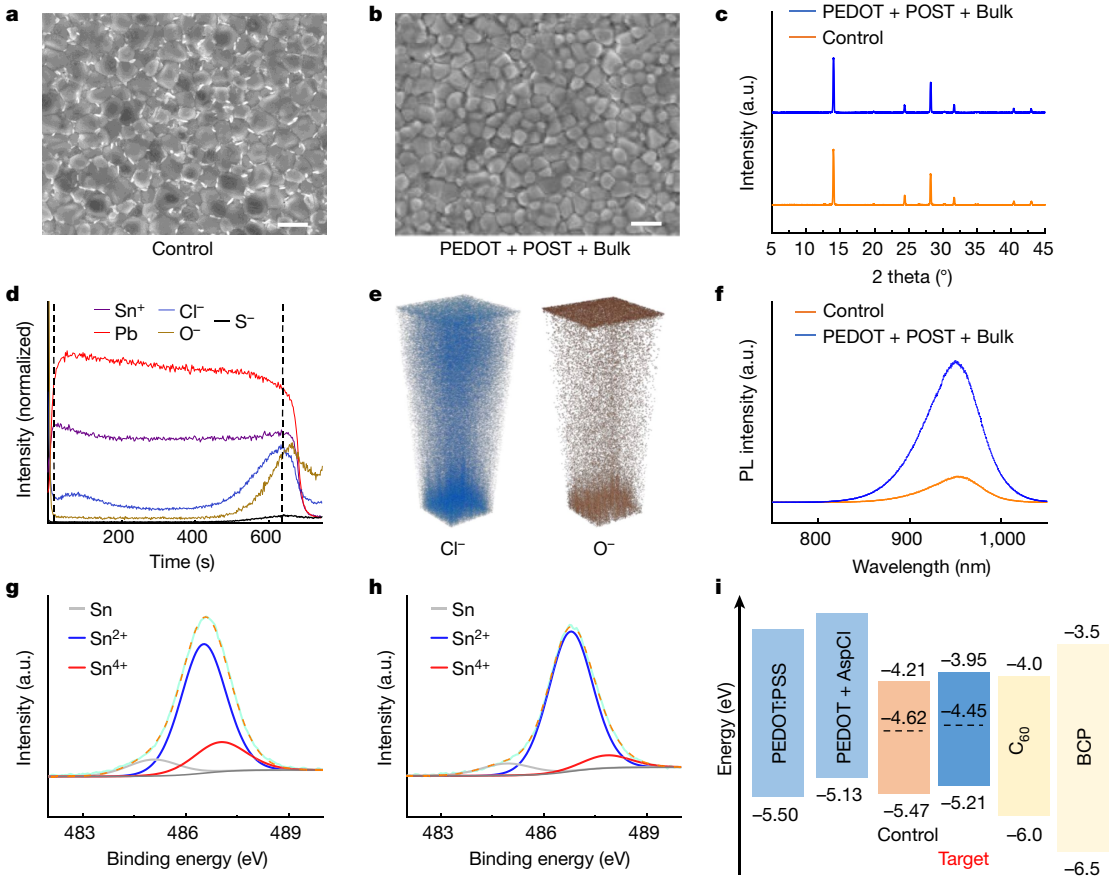

Fig. 2 | Characterization of NBG Sn–Pb perovskite films. a, Top-view SEM images of a control perovskite film. **b**, Top-view SEM images of a PEDOT + POST + Bulk AspCl-modified perovskite film. Scale bar, 1 µm. **c**, XRD patterns of the corresponding films. **d**,**e**, ToF-SIMS depth profile (**d**) and mapping image (**e**) of O^- and Cl^- for a PEDOT + POST + Bulk AspCl-modified perovskite film. **f**, Photoluminescence spectra of a control film and a PEDOT + POST + Bulk AspCl-modified film. **g**,**h**, XPS spectra of a control film (**g**) and XPS spectra (**h**) of a PEDOT + POST + Bulk AspCl-modified film. The integrated area ratios of Sn^{2+} and Sn^{4+} peaks for the control and PEDOT + POST + Bulk samples were approximately 3.7 and 10.0, respectively. **i**, Energy-level diagram of the devices based on Sn–Pb perovskites without or with multiple AspCl modifications.

resulting from the introduction of AspCl. Time-of-flight secondary-ion mass spectrometry (ToF-SIMS) results revealed that while the O^- and Cl^- were distributed throughout the perovskite films (Fig. 2d,e and Supplementary Fig. 16), they were mainly concentrated at the top and bottom interfaces because of the strong bonding of AspCl–SnI_2/PbI_2 and AspCl–AspCl, as demonstrated by DFT calculations. Bias and light-soaking stability tests on devices confirmed the capacity of AspCl to hinder ion migration (Supplementary Figs. 17 and 18). Additionally, the presence of Cl in AspCl elevated the activation energy required for I ion migration, further contributing to the suppression of ion migration[18,20]. Therefore, the multiple modifications with AspCl can effectively suppress ion migration and passivate defects. The photoluminescence intensity of the perovskite films was significantly enhanced after AspCl treatment (Fig. 2f and Supplementary Fig. 19), demonstrating that the use of AspCl can effectively suppress non-radiative recombination in the perovskite films[30]. To investigate the charge carrier dynamics within the films, we also performed transient absorption spectroscopy measurements on the samples (Supplementary Fig. 20). Notably, the introduction of AspCl led to a slowed decay profile, signifying an extended lifetime of photoinduced carriers within the Sn–Pb perovskite films[31,32].

X-ray photoelectron spectroscopy (XPS) measurements were further carried out to explore changes in the chemical environment and potential bonding of perovskites. As presented in Fig. 2g,h and Supplementary Fig. 21, a shift in the binding energy of Sn^{2+} and Sn^{4+} indicated the interaction between AspCl and perovskites[33,34]. Moreover, the integrated area ratio of Sn^{2+} and Sn^{4+} peaks for the PEDOT + POST + Bulk sample was the lowest, indicating reduced amounts of Sn^{4+} in the AspCl-incorporated perovskite films. To unravel the underlying mechanisms, we introduced AspCl separately into SnI_4 and SnI_2 solutions (Supplementary Fig. 14), demonstrating that AspCl could have a strong interaction with both SnI_4 and SnI_2, inhibiting the oxidation of Sn^{2+}. The presence of AspCl in the final perovskite films was also verified by XPS spectra of Cl (Supplementary Fig. 22).

To assess carrier recombination in the devices, we measured the slopes of the light intensity (P)-dependent open-circuit voltage (V_{oc}) curves. (Supplementary Fig. 23a). The decrease in n values suggested reduced Shockley–Read–Hall recombination in AspCl-incorporated PSCs[35]. We also measured the slopes of the P-dependent short-circuit current density (J_{sc}) curves of the devices. The n value calculated from the PEDOT + POST + Bulk device was closer to 1 than that of the other samples (Supplementary Fig. 23b), indicating suppressed interfacial recombination and enhanced carrier extraction in the PEDOT + POST + Bulk device[36]. Capacitance–voltage measurements for built-in potential (V_{bi}) demonstrated that the PEDOT + POST + Bulk sample exhibited the highest V_{bi} among the devices (Supplementary Fig. 24), consistent with the trend of V_{oc}, which facilitated carrier transport and separation and reduced carrier recombination[37]. Electrochemical impedance spectroscopy (EIS) measurements were further carried out to analyse charge transport characteristics of the devices (Supplementary Fig. 25). The PEDOT + POST + Bulk sample showed

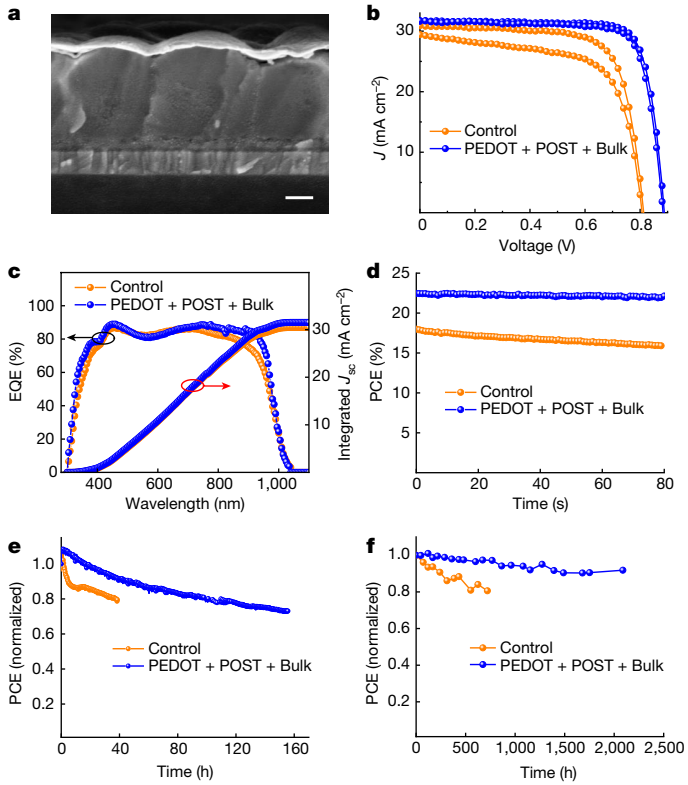

Fig. 3 | Performance of single-junction NBG Sn–Pb PSCs. a, Cross-sectional SEM image of a device with multiple AspCl modifications. Scale bar, 200 nm. **b**, *J*–*V* curves of the best-performing control and PEDOT + POST + Bulk AspCl-modified solar cells. **c**,**d**, EQE spectra (**c**) and SPO efficiencies (**d**) of the corresponding solar cells. **e**, Long-term MPP tracking of unencapsulated control (initial efficiency: 17.05%) and target (initial efficiency: 20.21%) solar cells under constant 1 sun (a light-emitting diode light source, equivalent to a global horizontal irradiance spectrum AM 1.5 G, 100 mW cm^{-2}) illumination in an N_2-filled glovebox at 55 °C. **f**, Long-term shelf-storage stability of encapsulated control (initial efficiency: 18.19%) and target (initial efficiency: 20.34%) devices stored in an N_2-filled glovebox at room temperature.

the largest semicircle compared with the other devices, implying the highest carrier recombination resistance and the lowest recombination rate[38]. Additionally, we measured space charge limited currents (SCLC) of the devices (Supplementary Fig. 26), indicating that the PEDOT + POST + Bulk (target) sample had the lowest trap density (N_t). These findings further validated that the incorporation of AspCl can reduce defects in Sn–Pb perovskites. As the energy levels of perovskites play a critical role in carrier separation and transport, we investigated the device band structure. To explore the conduction band minimum (CBM) and valence band maximum (VBM) levels of the films, we measured UV photoelectron spectroscopy (UPS) spectra and optical bandgaps (E_g) of different perovskite films (Supplementary Figs. 27–29). The introduction of AspCl caused favourable band alignment with C_{60} and PEDOT:PSS, ultimately leading to improved carrier separation and transport and consequently increased V_{oc} of devices[39] (Fig. 2i). Furthermore, Kelvin probe force microscopy (KPFM) measurements were performed to evaluate the work function change in different perovskite films (Supplementary Fig. 30), which were consistent with the UPS results.

Performance of single-junction NBG PSCs

Based on the above results, the resulting solar cells demonstrated improved performance. Fig. 3a and Supplementary Fig. 31 present cross-sectional SEM images of the devices employing control and target perovskite films, revealing similar morphology. Fig. 3b compares the *J*–*V* curves of the best-performing control and target devices. The J_{sc}, V_{oc}, fill factor (FF) and power conversion efficiency (PCE) derived from the *J*–*V* curves of the optimal control PSC were 30.99 (29.58) mA cm^{-2}, 0.81 (0.81) V, 72.35 (65.69)% and 18.20 (15.74)%, respectively, when measured from a reverse (forward) voltage scan. For comparison, the optimal target PSC had significantly improved J_{sc}, V_{oc}, FF, and PCE values of 31.69 (31.77) mA cm^{-2}, 0.89 (0.88) V, 79.90 (77.96)% and 22.46 (21.80)%, respectively. An independent laboratory also certified a comparable PCE of 21.72% (Supplementary Fig. 32). The integrated J_{sc} values derived from external quantum efficiency (EQE) curves of the control and target cells were 30.47 mA cm^{-2} and 31.51 mA cm^{-2} (Fig. 3c), respectively, which were consistent with the J_{sc} values obtained from the *J*–*V* curves (Fig. 3b). The steady-state output (SPO) efficiencies of the corresponding control and target devices at the maximum power points were 15.91% and 22.14% (Fig. 3d), respectively, which were also in line with the values determined from the *J*–*V* curves (Fig. 3b). Besides efficiency, the stability of solar cells was also improved by AspCl modification. The maximum power point (MPP) tracking stability tests of the devices under constant 1-sun illumination in Fig. 3e revealed that the target device without encapsulation retained 80% of its initial efficiency after 100 h of operation in an N_2-filled glovebox at 55 °C. By contrast, the control device retained 80% of its primitive efficiency after only 30 h of operation under the same conditions. Figure 3f displays the shelf-storage stability of the devices that were encapsulated and stored in an N_2-filled glovebox. After 2,000 h of storage at room temperature, the PCE of the target sample dropped to 92% of its original value, whereas the PCE of the control device had already decreased to 80% of its initial value after only 750 h under the same conditions. These results demonstrate that AspCl addition significantly enhanced both the efficiency and stability of Sn–Pb PSCs.

Performance of all-perovskite tandems

We then fabricated monolithic two-terminal (2T) all-perovskite tandem solar cells using NBG Sn–Pb PSCs as the bottom subcells and WBG ($FA_{0.8}Cs_{0.2}PbI_{1.8}Br_{1.2}$) PSCs as the top subcells (Fig. 4a,b). Supplementary Fig. 33 and Supplementary Table 6 provide *J*–*V* curves and corresponding parameters of an opaque single-junction WBG solar cell. Ultimately, our best-performing tandem device exhibited a high J_{sc} of 16.02 (16.06) mA cm^{-2}, V_{oc} of 2.11 (2.12) V, FF of 82.20 (78.47)% and PCE of 27.84 (26.75)% when measured under a reverse (forward) voltage scan (Fig. 4c), coupled with an SPO efficiency of 27.62% (Fig. 4d). An independent laboratory also certified comparable efficiencies of 27.34% and 27.12% with reverse and forward voltage scanning, respectively (Supplementary Fig. 34). The J_{sc} values of the bottom NBG and top WBG subcells integrated from EQE spectra (Fig. 4e) were in agreement with the J_{sc} values obtained from *J*–*V* measurements and certification results. Figure 4f and Supplementary Fig. 35 also provide statistics of photovoltaic parameters for thirty-two 2T all-perovskite tandem solar cells, showing good reproducibility. The long-term operational stability and shelf-storage stability of the devices are presented in Supplementary Fig. 36. The PCE of the unencapsulated tandem device retained 80% of its original PCE after 380 h of constant 1-sun irradiation at 55 °C. In addition, the encapsulated tandem device maintained 95% of its initial PCE after 2,000 h of storage in an N_2 atmosphere at room temperature, demonstrating its potential for the production of high-efficiency and good-stability tandem solar cells in the future.

Online content

Any methods, additional references, Nature Portfolio reporting summaries, source data, extended data, supplementary information,

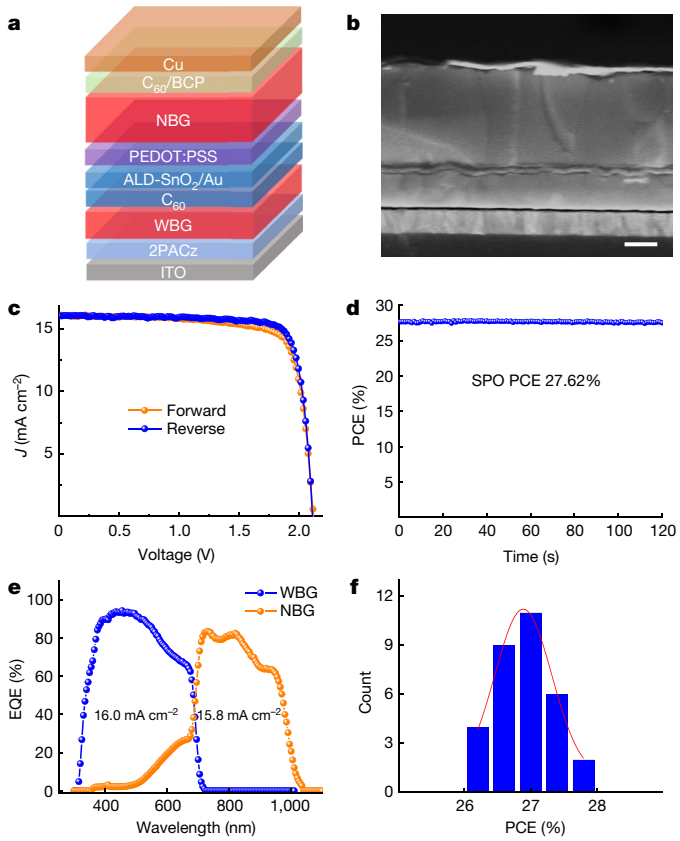

Fig. 4 | Performance of 2T all-perovskite tandem solar cells. a, Device structure diagram of tandem solar cells. **b**, Cross-sectional SEM image of a representative tandem solar cell. Scale bar, 300 nm. **c**, *J*–*V* curves of the best-performing tandem device measured under different voltage scan directions. **d**, SPO efficiency of the best-performing tandem solar cell. **e**, EQE spectra of the bottom subcell and top subcell. **f**, PCE statistics of thirty-two 2T tandem solar cells, which achieved an average PCE of 26.89 ± 0.43%. ALD, atomic layer deposition; 2PACz, [2-(9H-carbazol-9-yl)ethyl]phosphonic acid.

acknowledgements, peer review information; details of author contributions and competing interests; and statements of data and code availability are available at https://doi.org/10.1038/s41586-023-06707-z.

1. He, R. et al. Wide-bandgap organic–inorganic hybrid and all-inorganic perovskite solar cells and their application in all-perovskite tandem solar cells. *Energy Environ. Sci.* **14**, 5723–5759 (2021).
2. He, R. et al. All-perovskite tandem 1 cm^2 cells with improved interface quality. *Nature* **618**, 80–86 (2023).
3. Zhang, W. et al. Revealing key factors of efficient narrow-bandgap mixed lead-tin perovskite solar cells via numerical simulations and experiments. *Nano Energy* **96**, 107078 (2022).
4. Li, C. et al. Low-bandgap mixed tin–lead iodide perovskites with reduced methylammonium for simultaneous enhancement of solar cell efficiency and stability. *Nat. Energy* **5**, 768–776 (2020).
5. Tong, J. et al. Carrier control in Sn–Pb perovskites via 2D cation engineering for all-perovskite tandem solar cells with improved efficiency and stability. *Nat. Energy* **7**, 642–651 (2022).
6. Ke, W., Stoumpos, C. C. & Kanatzidis, M. G. "Unleaded" perovskites: status quo and future prospects of tin-based perovskite solar cells. *Adv. Mater.* **31**, 1803230 (2019).
7. Lin, R. et al. All-perovskite tandem solar cells with 3D/3D bilayer perovskite heterojunction. *Nature* **620**, 994–1000 (2023).
8. Yoo, J. J. et al. Efficient perovskite solar cells via improved carrier management. *Nature* **590**, 587–593 (2021).
9. Liao, W. et al. Fabrication of efficient low-bandgap perovskite solar cells by combining formamidinium tin iodide with methylammonium lead iodide. *J. Am. Chem. Soc.* **138**, 12360–12363 (2016).
10. Huang, L. et al. Efficient narrow-bandgap mixed tin-lead perovskite solar cells via natural tin oxide doping. *Adv. Mater.* **35**, 2301125 (2023).
11. Jiang, Q. et al. Compositional texture engineering for highly stable wide-bandgap perovskite solar cells. *Science* **378**, 1295–1300 (2022).
12. Tong, J. et al. Carrier lifetimes of >1 μs in Sn-Pb perovskites enable efficient all-perovskite tandem solar cells. *Science* **364**, 475–479 (2019).
13. Lin, R. et al. All-perovskite tandem solar cells with improved grain surface passivation. *Nature* **603**, 73–78 (2022).
14. Xiao, K. et al. All-perovskite tandem solar cells with 24.2% certified efficiency and area over 1 cm^2 using surface-anchoring zwitterionic antioxidant. *Nat. Energy* **5**, 870–880 (2020).
15. Wang, Z. et al. Suppressed phase segregation for triple-junction perovskite solar cells. *Nature* **618**, 74–79 (2023).
16. Chen, H. et al. Regulating surface potential maximizes voltage in all-perovskite tandems. *Nature* **613**, 676–681 (2023).
17. Saidaminov, M. I. et al. Suppression of atomic vacancies via incorporation of isovalent small ions to increase the stability of halide perovskite solar cells in ambient air. *Nat. Energy* **3**, 648–654 (2018).
18. Chen, B., Rudd, P. N., Yang, S., Yuan, Y. & Huang, J. Imperfections and their passivation in halide perovskite solar cells. *Chem. Soc. Rev.* **48**, 3842–3867 (2019).
19. Liu, C. et al. Highly efficient quasi-2D green perovskite light-emitting diodes with bifunctional amino acid. *Adv. Opt. Mater.* **10**, 2200276 (2022).
20. Xu, J. et al. Triple-halide wide-band gap perovskites with suppressed phase segregation for efficient tandems. *Science* **367**, 1097–1104 (2020).
21. Li, G. et al. Ionic liquid stabilizing high-efficiency tin halide perovskite solar cells. *Adv. Energy Mater.* **11**, 2101539 (2021).
22. Zheng, X. et al. Quantum dots supply bulk- and surface-passivation agents for efficient and stable perovskite solar cells. *Joule* **3**, 1963–1976 (2019).
23. Liu, F. et al. Is Excess PbI_2 beneficial for perovskite solar cell performance? *Adv. Energy Mater.* **6**, 1502206 (2016).
24. Jiang, Q. et al. Planar-structure perovskite solar cells with efficiency beyond 21%. *Adv. Mater.* **29**, 1703852 (2017).
25. Ke, W. et al. Employing lead thiocyanate additive to reduce the hysteresis and boost the fill factor of planar perovskite solar cells. *Adv. Mater.* **28**, 5214–5221 (2016).
26. Tumen-Ulzii, G. et al. Detrimental effect of unreacted PbI_2 on the long-term stability of perovskite solar cells. *Adv. Mater.* **32**, 1905035 (2020).
27. Hu, S. et al. Optimized carrier extraction at interfaces for 23.6% efficient tin–lead perovskite solar cells. *Energy Environ. Sci.* **15**, 2096–2107 (2022).
28. Yokoyama, T. et al. Overcoming short-circuit in lead-free $CH_3NH_3SnI_3$ perovskite solar cells via kinetically controlled gas–solid reaction film fabrication process. *J. Phys. Chem. Lett.* **7**, 776–782 (2016).
29. Li, P. et al. Ligand engineering in tin-based perovskite solar cells. *Nanomicro Lett.* **15**, 167 (2023).
30. Shao, W. et al. Modulation of nucleation and crystallization in PbI_2 films promoting preferential perovskite orientation growth for efficient solar cells. *Energy Environ. Sci.* **16**, 252–264 (2023).
31. Ye, F. et al. Roles of MACl in sequentially deposited bromine-free perovskite absorbers for efficient solar cells. *Adv. Mater.* **33**, 2007126 (2021).
32. Liu, Y. et al. A generic lanthanum doping strategy enabling efficient lead halide perovskite luminescence for backlights. *Sci. Bull.* **68**, 1017–1026 (2023).
33. Lee, J.-W. et al. Formamidinium and cesium hybridization for photo- and moisture-stable perovskite solar cell. *Adv. Energy Mater.* **5**, 1501310 (2015).
34. Liao, Y. et al. Highly oriented low-dimensional tin halide perovskites with enhanced stability and photovoltaic performance. *J. Am. Chem. Soc.* **139**, 6693–6699 (2017).
35. Glowienka, D. & Galagan, Y. Light intensity analysis of photovoltaic parameters for perovskite solar cells. *Adv. Mater.* **34**, 2105920 (2022).
36. Huang, Z., Hu, X., Liu, C., Tan, L. & Chen, Y. Nucleation and crystallization control via polyurethane to enhance the bendability of perovskite solar cells with excellent device performance. *Adv. Funct. Mater.* **27**, 1703061 (2017).
37. Kapil, G. et al. Tin-lead perovskite fabricated via ethylenediamine interlayer guides to the solar cell efficiency of 21.74%. *Adv. Energy Mater.* **11**, 2101069 (2021).
38. Kuan, C. H. et al. Dopant-free pyrrolopyrrole-based (PPr) polymeric hole-transporting materials for efficient tin-based perovskite solar cells with stability over 6000 h. *Adv. Mater.* **35**, 2300681 (2023).
39. Wang, J. et al. Carbazole-based hole transport polymer for methylammonium-free tin–lead perovskite solar cells with enhanced efficiency and stability. *ACS Energy Lett.* **7**, 3353–3361 (2022).

Methods

DFT calculations

AspCl–PbI_2, AspCl–SnI_2, FAI–PbI_2, FAI–SnI_2, AspCl–AspCl, AspCl–FAI and FAI–FAI calculated results were obtained by using the DMol 3 module in Materials Studio[40]. The basic parameters of calculation were: the exchange correlation functional was the Perdew–Burke–Ernzerh (PBE) method in the generalized gradient function (GGA), the numerical base group was set to double numerical plus polarization 3.5, and the orbital cutoff precision was fine. The energy convergence accuracy was 1.0×10^{-5} Ha, the maximum force convergence was 0.002 Ha $Å^{-1}$ and the maximum displacement convergence accuracy was 0.005 Å. Grimme-D2 (ref. 41) was chosen for van der Waals interactions.

AspCl orientations on different substrates (perovskite, C_{60} and PEDOT:PSS) were calculated with the Vienna ab initio simulation package[42,43]. The core–valence interaction was described by the projector-augmented wave method[44,45]. The cutoff energy for basis functions was 520 eV. The GGA of the PBE functional was used for exchange correlation[46]. The Grimme's DFT-D3 scheme was employed for the inclusion of van der Waals interactions[47]. All atoms were relaxed until the Hellmann–Feynman forces on them were below 0.01 eV $Å^{-1}$. For perovskite slab adsorption calculations, the Γ-only k-point mesh was chosen, and dipole correction was also considered. The slab was separated by a vacuum layer of 25 Å to avoid potential interaction between adjacent layers. The interactions between AspCl and C_{60} or PEDOT were simulated within a box of 30 × 30 × 30 Å.

Materials

All chemicals without further purification were used for preparing perovskite precursors. FAI (99.9%), methylammonium iodide (MAI, 99.9%), SnI_2 (99.99%) and ITO (12 Ω sq^{-1}) were purchased from Advanced Election Technology Co., Ltd. Tin fluoride (SnF_2, 98%), N, *N*-dimethylformamide (DMF, 99.8%), dimethyl sulphoxide (DMSO, 99.8%), isopropanol (IPA, 99.8%), chlorobenzene (CB, 99.8%), and lead thiocyanate ($Pb(SCN)_2$,99.5%) were bought from Sigma Aldrich (Shanghai) Trading Co., Ltd. C_{60} (99.9%) and Copper (Cu) were purchased from Xi'an Yuri Solar Co., Ltd. PbI_2 (99.99%) was bought from Tokyo Chemical Industry (Shanghai) development Co., Ltd. PEDOT:PSS was purchased from Heraeous Germany Co., Ltd. BCP (99.5%) was purchased from Jilin OLED Material Tech Co., Ltd. Asp (98%) was bought from Bide Pharmatech Co., Ltd.

Preparation of AspCl

Mixtures of Asp and HCl with a molar ratio of 1:1.1 were added to a reagent bottle. The solution was stirred for 3 h to dissolve Asp and then heated to 180 °C for 6 h to evaporate the solvents. Finally, AspCl powders were obtained after the reagent bottle was heated in an oven for 1 day at 70 °C.

Preparation of HTL solutions

HTL solutions were gained by adding approximately 0–10 mg of AspCl to 1 ml of PEDOT:PSS solutions, and the solutions were stirred for 2 h at room temperature. Then, the HTL solutions were filtered by a 0.45 μm filter before use.

Preparation of posttreatment solutions

To prepare posttreatment solutions with different concentrations, 0–10 mg AspCl was dissolved in 1 ml of IPA. The solutions were stirred for 3 h at room temperature before use.

Preparation of precursor solutions

WBG $FA_{0.8}Cs_{0.2}PbI_{1.8}Br_{1.2}$ perovskite precursors with a concentration of 1.1 M were prepared by dissolving FAI, CsI, PbI_2, $PbBr_2$ and $Pb(SCN)_2$ in a mixed solvent of DMF and DMSO with a volume ratio of 3:1. The molar ratio of FAI:CsI was 4:1 and the molar ratio of PbI_2:$PbBr_2$:$Pb(SCN)_2$ was 2:3:0.02. The precursors were stirred at 70 °C for 3 h before use.

NBG $FA_{0.7}MA_{0.3}Pn_{0.5}Sn_{0.5}I_3$ perovskite precursor solutions with a concentration of 1.8 M were prepared by dissolving FAI, MAI, PbI_2, SnI_2, AspCl, SnF_2 and $Pb(SCN)_2$ in a mixed solvent of DMF and DMSO with a volume ratio of 3:1. The molar ratio of FAI:MAI was 7:3 and the molar ratio of PbI_2:SnI_2:AspCl:SnF_2:$Pb(SCN)_2$ was 1:1:0–0.25:0.1:0.02. The precursors were stirred at 25 °C for 3 h before use.

Fabrication of single-junction NBG PSCs

The etched ITO substrates were ultrasonically cleaned by detergent, deionized water, acetone, IPA and ethanol for 15 min, respectively. Before depositing HTLs, the ITO substrates were exposed to UV ozone for 15 min. Next, PEDOT:PSS solutions were spin-coated onto the substrates at 5,000 rpm for 30 s and annealed at 140 °C for 30 min. After annealing, the substrates were immediately transferred into an N_2-filled glovebox. The perovskite precursors after filtering were directly deposited onto the substrates using a one-step spin-coating method at 1,000 rpm for 10 s and 4,000 rpm for 40 s. A quantity of 400 μl of CB was dropped onto the films at the twentieth second before the end of spin-coating. The substrates with perovskite films were annealed at 100 °C for 10 min. In the following, the posttreatment solutions were spin-coated onto the perovskite films at 4,000 rpm for 30 s, and the films were annealed at 100 °C for 7 min. Finally, C_{60} (20 nm), BCP (7 nm) and Cu (80 nm) were subsequently deposited on the perovskite films by a thermal evaporator (Wuhan PDVacuum Technologies Co., Ltd).

Fabrication of single-junction WBG PSCs

The etched ITO glass substrates were ultrasonically cleaned with detergent, deionized water, acetone, IPA and ethanol for 15 min, respectively. Before depositing HTLs, the ITO substrates were exposed to UV ozone for 15 min. Then, the substrates were immediately transferred into an N_2-filled glovebox. A 2PACz solution (0.3 mg ml^{-1}) was spin-coated onto the ITO substrates at 3,000 rpm for 30 s and annealed at 100 °C for 10 min. After that, the perovskite precursor solutions were spin-coated at 4,000 rpm for 30 s. At the tenth second before the end of spin-coating, 500 μl of diethyl ether was dropped onto the centre of the films. The perovskite films were annealed at 70 °C for 2 min and 100 °C for 8 min. Then propane-1,3-diammonium iodide solutions were spin-coated onto the perovskite films at 4,000 rpm for 30 s and annealed at 100 °C for 5 min (ref. 16). The films were transferred to a thermal evaporator chamber after the posttreatment, and 20 nm of C_{60} was thermally deposited. Next, the substrates were placed in an ALD system to deposit a 20-nm-thick (130 cycles) SnO_2 layer at 90 °C. Finally, the substrates were coated with 80 nm of Cu by a thermal evaporator (Wuhan PDVacuum Technologies Co., Ltd).

Fabrication of 2T all-perovskite tandem solar cells

WBG subcells were first assembled using the same processes as the fabrication of single-junction WBG PSCs until the step of the ALD-SnO_2 layer. Then, the substrates were transferred to a thermal evaporator (Wuhan PDVacuum Technologies Co., Ltd) to deposit a 1-nm-thick Au interlayer. NBG subcells were then deposited on top of the substrates, following the same processes as the fabrication of single-junction NBG PSCs.

Device performance measurements

J–*V* measurements were performed using a Keithley 2400 source meter and a solar simulator (SS-X50, Enlitech) along with AM 1.5 G spectra. The intensity of the spectra was calibrated using a certified WPVS standard solar reference cell (SRC-2020, Enlitech; traceable to the National Renewable Energy Laboratory) at 100 mW cm^{-2}. Bias voltages for *J*–*V* measurements for single-junction cells were scanned from −0.1 V to 1 V and from 1 V to −0.1 V with a scanning rate of 0.2 V s^{-1}, a voltage step of 50 mV and a delay time of 25 ms. Bias voltages for *J*–*V* measurements

for tandem cells were scanned from −0.1 V to 2.2 V and from 2.2 V to −0.1 V with a scanning rate of 0.2 V s^{-1}, a voltage step of 50 mV and a delay time of 25 ms. The device area was 0.0948 cm^2 and was masked with a metal aperture to define an active area of 0.070225 cm^2. EQE spectra were measured using a quantum efficiency/incident photon to current conversion efficiency system (Enli Technology Co., Ltd). For EQE measurements of tandem solar cells, two light-emitting diodes with emission wavelengths at 450 nm and 850 nm were used as the bias lights to measure NBG and WBG subcells, respectively.

Scanning electron microscopy measurements

Film morphology and cross-sectional structures of devices were collected with a Zeiss SIGMA field-emission scanning electron microscope.

Film X-ray diffraction measurements

The structures of perovskites were examined using a Rigaku smartlab XRD with Cu Kα radiation under operating conditions of 40 kV and 44 mA. All samples for XRD testing were prepared on ITO substrates.

X-ray photoelectron spectroscopy and ultraviolet photoelectron spectroscopy measurements

XPS and UPS spectra were performed using an XPS/UPS system (ESCLAB 250Xi, Thermo Scientific). The XPS used monochromatic Mg Kα radiation as the excitation source. XPS spectra were fitted using the Thermo Avantage software. Preceding the fitting process, energy levels were meticulously calibrated, with the reference C1s level set at 284.6 eV. When fitting the tin peaks, the full-widths at half-maximum of Sn, Sn^{2+} and Sn^{4+} were consistently aligned. Moreover, considering the observed shifts in XPS spectra upon AspCl doping, we endeavoured to sustain a fixed separation between Sn, Sn^{2+} and Sn^{4+} peaks across all curves, to best accommodate the total Sn curves. Finally, the Thermo Advantage software automatically calculated the area ratios of Sn^{2+} and Sn^{4+} by integrating the respective peak areas. UPS used He Iα radiation. The work function (W_f) of samples was calculated using the equation of $E_f = 21.22\ eV - E_{cutoff}$, where E_f is the Fermi level and E_{cutoff} is the cutoff of the UPS spectra in the high-binding energy range. The difference between the VBM (E_{VBM}) and E_f was extracted from the cutoff of UPS spectra in the low binding energy range, and the conduction band minimum (E_{CBM}) was calculated using the equation of $E_{CBM} = E_{VBM} + E_g$, where E_g is the optical bandgap.

Atomic force microscopy and Kelvin probe force microscopy measurements

AFM height images and KPFM potential distribution images were obtained in the ambient atmosphere using a Bruker Dimension Icon XR AFM. In the KPFM measurements, the voltages were applied to the samples and the contact electrical potential difference (CPD) was consistent with the work function of the samples. Thus, a higher CPD value represented a higher work function, indicating a deeper Fermi level.

Transient absorption measurements

Transient absorption spectra were measured using an ultrafast transient absorption spectrometer (HARPIA, Light Conversion). In this system, the output of a femtosecond laser (a repetition rate of 40 kHz, a central wavelength of 690 nm and a pulse duration of approximately 120 fs, PHAROS, Light Conversion) was split into two parts: one passed through the optical parametric amplification (ORPHEUS twins, Light Conversion) and became a pump pulse to excite perovskite thin films; the other passed through the delay stage and produced white light via sapphire and then acted as the probe beam. The pump and probe light focused on the samples with a spot size of about 64 μm. Owing to the small angle between these two beams, the pump pulse was blocked by a pinhole, and the probe was collected with a spectrometer.

Other characterizations

Absorption spectra were measured using a SHIMADZU mini 1280 UV-vis spectrophotometer. Steady-state photoluminescence measurements were performed with a DeltaFlex fluorescence spectrometer (HORIBA) using an excitation source of a 481 nm picosecond-pulsed diode laser. Electrochemical impedance spectra were recorded using a CHI 770E electrochemical workstation (Shanghai Chenhua Instruments, China) in a frequency range of 1 MHz to 1 Hz with a bias of 0 V in the dark. TOF-SIMS (Tescan AMBER) spectrometer was used for depth profile analysis of perovskites with 30 KV and 30 pA.

Reporting summary

Further information on research design is available in the Nature Portfolio Reporting Summary linked to this article.

Data availability

All data are available in the main text or supplementary materials. The data and code that support the findings of this study are available from the corresponding authors on request.

40. Clark, S. J. et al. First principles methods using CASTEP. *Z. Kristallogr. Cryst. Mater.* **220**, 567–570 (2005).
41. Grimme, S. Semiempirical GGA-type density functional constructed with a long-range dispersion correction. *J. Comput. Chem.* **27**, 1787–1799 (2006).
42. Kresse, G. & Hafner, J. Ab initio molecular dynamics for liquid metals. *Phys. Rev. B* **47**, 558–561 (1993).
43. Kresse, G. & Furthmüller, J. Efficient iterative schemes for ab initio total-energy calculations using a plane-wave basis set. *Phys. Rev. B* **54**, 11169–11186 (1996).
44. Blöchl, P. E. Projector augmented-wave method. *Phys. Rev. B* **50**, 17953–17979 (1994).
45. Kresse, G. & Joubert, D. From ultrasoft pseudopotentials to the projector augmented-wave method. *Phys. Rev. B* **59**, 1758–1775 (1999).
46. Perdew, J. P., Burke, K. & Ernzerhof, M. Generalized gradient approximation made simple. *Phys. Rev. Lett.* **77**, 3865–3868 (1996).
47. Grimme, S., Antony, J., Ehrlich, S. & Krieg, H. A consistent and accurate ab initio parametrization of density functional dispersion correction (DFT-D) for the 94 elements H-Pu. *J. Chem. Phys.* **132**, 154104 (2010).

Acknowledgements This work was supported by Key Lab of Artificial Micro- and Nanostructures of Ministry of Education of China, Wuhan University. We thank the Core Facility of Wuhan University for SEM, ToF-SIMS and XPS measurements. We also acknowledge the financial support from the National Natural Science Foundation of China (Grant Numbers: 12174290, 12134010) and the Natural Science Foundation of Hubei Province, China (Grant Number: 2021CFB039).

Author contributions S.Z. and W.K. conceived the idea and designed the experiments. S.Z., S.F. and Chen W. developed tandem solar cells. W.M. performed DFT calculation and theoretical analysis. J.Z. conducted SCLC measurements. Y.Z. performed EIS characterization and analysis. D.P. characterized the surface and cross-section morphology of perovskite films and devices. Q.L. participated in the optimization of single-junction NBG and tandem solar cells. Cheng W. and T.W. conducted photoluminescence and transient absorption measurements and analysis. L.H. conducted XPS measurements and analysis. H.G. conducted ToF-SIMS and KPFM measurements and their analysis. W.Z. conducted the long-term device stability measurements and analysis. G.Z. conducted tandem EQE measurements. K.D. and H.C. conducted XRD measurements and their analysis. S.W. conducted UPS and absorption measurements. S.Z. and W.K. wrote the first draft of the manuscript. All authors discussed the results and contributed to the revisions of the manuscript. G.F. and W.K. supervised the project.

Competing interests The authors declare no competing interests.

Additional information

Supplementary information The online version contains supplementary material available at https://doi.org/10.1038/s41586-023-06707-z.

Correspondence and requests for materials should be addressed to Guojia Fang or Weijun Ke.

Peer review information *Nature* thanks Jiangzhao Chen and the other, anonymous, reviewer(s) for their contribution to the peer review of this work.

nature research

Corresponding author(s): Weijun Ke, Guojia Fang

Solar Cells Reporting Summary

Nature Research wishes to improve the reproducibility of the work that we publish. This form is intended for publication with all accepted papers reporting the characterization of photovoltaic devices and provides structure for consistency and transparency in reporting. Some list items might not apply to an individual manuscript, but all fields must be completed for clarity.

For further information on Nature Research policies, including our data availability policy, see Authors & Referees.

Experimental design

Please check: are the following details reported in the manuscript?

1. Dimensions			
Area of the tested solar cells	☒ Yes ☐ No	Methods Section, Device performance measurements. "The device area was 0.0948 cm2"
Method used to determine the device area	☒ Yes ☐ No	Methods Section, Device performance measurements. "The device area was 0.0948 cm2 and masked with a metal aperture to define an active area of 0.070225 cm2"
2. Current-voltage characterization			
Current density-voltage (J-V) plots in both forward and backward direction	☒ Yes ☐ No	Figure 3b, Figure 4c, Supplementary Figure 32-34 and Supplementary Table 4 and 6
Voltage scan conditions *For instance: scan direction, speed, dwell times*	☒ Yes ☐ No	Methods Section, Device performance measurements. "The J–V curves of both single-junction and tandem solar cells were taken with reverse and forward voltage scans with a scan speed of 0.2 V/s, a voltage step of 50 mV, and a delay time of 25 ms."
Test environment *For instance: characterization temperature, in air or in glove box*	☒ Yes ☐ No	at room temperature and in an N2-filled glove box.
Protocol for preconditioning of the device before its characterization	☐ Yes ☒ No	No preconditioning is required for our cell characterization
Stability of the J-V characteristic *Verified with time evolution of the maximum power point or with the photocurrent at maximum power point; see ref. 7 for details.*	☒ Yes ☐ No	Figure 3d, Figure 4d , stable power output efficiencies near the maximum power point voltages were provided.
3. Hysteresis or any other unusual behaviour			
Description of the unusual behaviour observed during the characterization	☒ Yes ☐ No	Negligible hysteresis was found.
Related experimental data	☒ Yes ☐ No	J-V curves under reverse and forward scans were provided.
4. Efficiency			
External quantum efficiency (EQE) or incident photons to current efficiency (IPCE)	☒ Yes ☐ No	EQE curves were provided in Figure 3c and Figure 4e.
A comparison between the integrated response under the standard reference spectrum and the response measure under the simulator	☒ Yes ☐ No	The integrated Jsc values obtained from EQE were agree well with the Jsc determined from the J–V measurements
For tandem solar cells, the bias illumination and bias voltage used for each subcell	☒ Yes ☐ No	Methods Section, Device performance measurements.
5. Calibration			
Light source and reference cell or sensor used for the characterization	☒ Yes ☐ No	Methods Section, Device performance measurements.

Confirmation that the reference cell was calibrated and certified	☒ Yes ☐ No	Methods Section, Device performance measurements. "The reference cell was certified by the certified WPVS standard solar reference cell (SRC-2020, Enlitech; traceable to NREL) at 100mW/cm2"
Calculation of spectral mismatch between the reference cell and the devices under test	☐ Yes ☒ No	The light spectrum used for measurements matches well with the reference silicon cell, and we did not calculate the spectral mismatch between the reference cell and the tested devices.

6. Mask/aperture

Size of the mask/aperture used during testing	☒ Yes ☐ No	0.070225 cm2
Variation of the measured short-circuit current density with the mask/aperture area	☐ Yes ☒ No	Negligible

7. Performance certification

Identity of the independent certification laboratory that confirmed the photovoltaic performance	☒ Yes ☐ No	A representative single-junction solar cell and a tandem cell were certified by Shanghai Institute of Measurement and Testing Technology (SIMT)
A copy of any certificate(s) *Provide in Supplementary Information*	☒ Yes ☐ No	Supplementary Fig. 32 and 34

8. Statistics

Number of solar cells tested	☒ Yes ☐ No	thirty-two for tandem devices
Statistical analysis of the device performance	☒ Yes ☐ No	Supplementary Figure 5, Supplementary Figure 6, Supplementary Figure 7 Supplementary Figure 35, Figure 4f

9. Long-term stability analysis

Type of analysis, bias conditions and environmental conditions *For instance: illumination type, temperature, atmosphere humidity, encapsulation method, preconditioning temperature*	☒ Yes ☐ No	Figure 3e, Figure 3f, Supplementary Figure 36 and their legends, Methods Section, Device performance measurements.